Research Square

Preprints are preliminary reports that have not undergone peer review.
They should not be considered conclusive, used to inform clinical practice,
or referenced by the media as validated information.

A predictive grinding force model for helical gear form grinding considering spatial geometric and kinematic characteristics

Shuying YANG

shuyingyang@cslg.edu.cn

Suzhou University of Technology

Lei ZHENG

Yifei DING

Weifang CHEN

Rupeng ZHU

Research Article

Keywords: Helical gear, Form grinding, Force model, Spatial geometric, Nonuniform distribution

Posted Date: July 10th, 2026

DOI: https://doi.org/10.21203/rs.3.rs-9845296/v1

License: This work is licensed under a Creative Commons Attribution 4.0 International License.
Read Full License

Version of Record: A version of this preprint was published at The International Journal of Advanced Manufacturing Technology on October 8th, 2026. See the published version at https://doi.org/10.1007/s00170-026-19140-z.

A predictive grinding force model for helical gear form grinding considering spatial geometric and kinematic characteristics

Shuying YANG[1, *], Lei ZHENG[1], Yifei DING[1], Weifang CHEN[2], Rupeng ZHU[2]

1 College of Mechanical Engineering, Suzhou University of Technology, Suzhou 215500, China

2 College of Mechanical and Electrical Engineering, Nanjing University of Aeronautics and Astronautics, Nanjing 210016, China

[*]Corresponding author: Shuying YANG, shuyingyang@cslg.edu.cn

Abstract

To examine the distribution and variation of grinding forces in helical gear form grinding, a theoretical grinding force model was constructed considering the spatial motion relationships, geometric contact characteristics, and grinding mechanism. The model constants were determined through grinding experiments, and the predicted forces were validated against the measured data under different process parameters. Theoretical and experimental measurements indicate that both normal and tangential grinding forces increase with the grinding depth and feed rate. Increasing the wheel speed reduces the tangential force, whereas the normal force shows a non-monotonic variation. Furthermore, the simulation reveals that grinding forces vary nonuniformly along the tooth profile, increasing with the involute rolling angle, decreasing with the transition arc angle, and peaking at the tooth root. These findings provide a theoretical framework for grinding parameter optimization in helical gear form grinding.

Keywords: Helical gear, Form grinding, Force model, Spatial geometric, Nonuniform distribution

1 Introduction

With the continuous development of high-performance transmission systems, stricter requirements have been imposed on the dimensional accuracy and surface integrity of gears. As a finishing operation capable of generating precise tooth profiles, form grinding is widely employed in the final manufacturing stage of hardened gears. During this process, the mechanical response during this process has emerged as one of the dominant factors affecting the operational reliability of gears [1]. Specifically, the grinding force acts as an important indicator of the interaction between the grains and workpiece surface, reflecting both the material removal process and the local contact load. It is also closely related to residual stress formation, surface roughness, and the overall integrity of the tooth flank[2][3]. Therefore, establishing a predictive grinding force model that can accurately describe the actual contact characteristics and tooth profile response is of great theoretical importance for machining parameter optimization and surface quality control in helical gear form grinding.

Significant progress has been achieved in grinding force modeling for processes such as surface grinding and cylindrical grinding, mainly because these operations feature relatively regular wheel–workpiece contact geometry and uniform local kinematics [4]. In contrast, form grinding presents an intricate coupling between the wheel profile and the tooth surface, producing a complex, time-varying three-dimensional contact region [5]. During this process, the local cutting speed, contact arc length, and instantaneous undeformed chip thickness vary continuously along the tooth surface, leading to strong spatial nonuniformity and temporal fluctuation of the grinding force [6]. Furthermore, the combined effects of wheel wear, profile errors, and multi-axis kinematic coupling intensify the nonlinear mechanical behavior in the contact region [7], making it difficult for traditional simplified models to accurately capture the actual force characteristics in form grinding.

Recent studies have intensively explored the kinematic and mechanical behavior of form

grinding, giving rise to a series of predictive models for grinding forces. Li et al. [8] proposed a coupled force–temperature model for turbine disk slot form grinding, revealing that uneven heat transfer caused the peak temperature at the slot edge to exceed that at the bottom by about 30%. Miao et al. [9] established a quantitative model linking tangential and normal forces in creep-feed form grinding of nickel-based superalloy blade roots to key process parameters such as wheel speed, feed rate, and grinding depth. Wu et al. [10] proposed an infinitesimal-based model for grinding forces on 2D freeform surfaces, reducing the complex form grinding process to multiple inclined flat grindings that capture sliding, plowing, and chip formation mechanisms.

For gear form grinding, the contact geometry varies spatially, with the equivalent wheel radius, wheel linear velocity, and normal grinding depth differ along the tooth profile. These complex geometric and kinematic interactions lead to strongly nonuniform grinding force distributions along the tooth surface, which cannot be captured by traditional models developed under uniform contact assumptions [11][12]. Xiao et al. [13] proposed a force model combining wheel topography, kinematics, and material removal mechanisms, accurately predicting forces and revealing the distinctive material removal features of gear form grinding compared with conventional surface grinding. Bie et al. [14] modeled grinding forces in two-dimensional ultrasonic vibration-assisted dry gear grinding, showing that ultrasonic excitation periodically reduces the applied forces by altering abrasive grain kinematics and force distribution. Based on the micro-scale interaction between abrasive grains and the workpiece, Yi et al. [15][16]developed a predictive grinding force model incorporating undeformed chip thickness, stochastic grain distribution, and material removal characteristics, achieving accurate prediction of tangential and normal force distributions. Yang et al. [17][18] established a model for involute spur gear form grinding using microcrystalline corundum wheels, analyzing the influence of process parameters, abrasive density, and geometrical factors on the grinding force, providing valuable theoretical and experimental insights. However, most existing models are limited to spur gears or two-dimensional simplifications, neglecting the spatial geometry and kinematic coupling inherent in helical gear form grinding.

This study develops a predictive model for full-tooth-height form grinding of involute helical gears to overcome the aforementioned limitation. The model explicitly considers the spatial kinematics and geometric contact of the helical surface and calculates the position-dependent equivalent wheel radius and grinding depth along the normal section. Using a unit-width plane grinding force model, the total tangential and normal forces are obtained through integration of local forces along the three-dimensional contact curve. Helical gear grinding experiments were performed to calibrate empirical coefficients and assess the accuracy of model predictions. Results indicate a highly nonuniform grinding force distribution along the tooth profile, reaching a minimum near the base circle and peaking at the root. Tangential and normal forces increase with greater radial grinding depth and feed rate; however, with higher wheel speed, the tangential force decreases and the normal force varies non-monotonically. The proposed model provides a foundation for process parameter optimization and surface integrity improvement during helical gear form grinding.

2 Spatial kinematic model of form grinding

In helical gear form grinding, the generation of the tooth surface results from the continuous relative motion between the profiled grinding wheel and the workpiece. The final tooth geometry is formed through an envelope mechanism associated with the wheel–gear contact path. Figure 1 illustrates the spatial kinematics of helical gear form grinding, which mainly consists of spindle rotation, tangential feed, and radial feed motions. During grinding, the wheel rotates at n_s with a

radial infeed for material removal, whereas the helical gear rotates at n_g and translates axially at a feed rate of v_w. In Fig.1, S_w (X_w, Y_w, Z_w) and S_s (X_s, Y_s, Z_s) denote coordinate systems attached to the gear and the wheel.

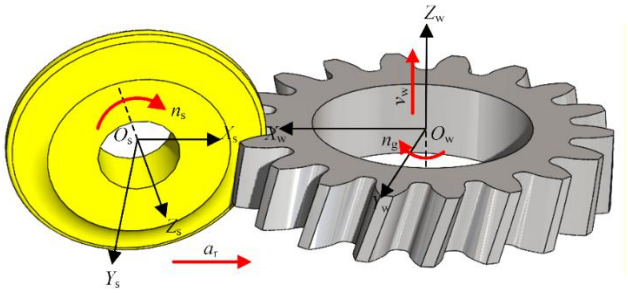


Fig.1 Kinematic representation of the helical gear form grinding process

As shown in Fig.2, a spatial motion coordinate framework of helical gear form grinding is established from the relative motion between the grinding wheel and the workpiece. S (X, Y, Z) denotes the stationary reference frame. At the initial grinding position, the coordinate system S_w (X_w, Y_w, Z_w) coincides with S (X, Y, Z), and the initial center distance between the wheel and gear is A. When the gear rotates by a unit angle at a speed of n_g, the wheel moves radially by a displacement A_x, thereby maintaining the prescribed meshing condition during material removal.

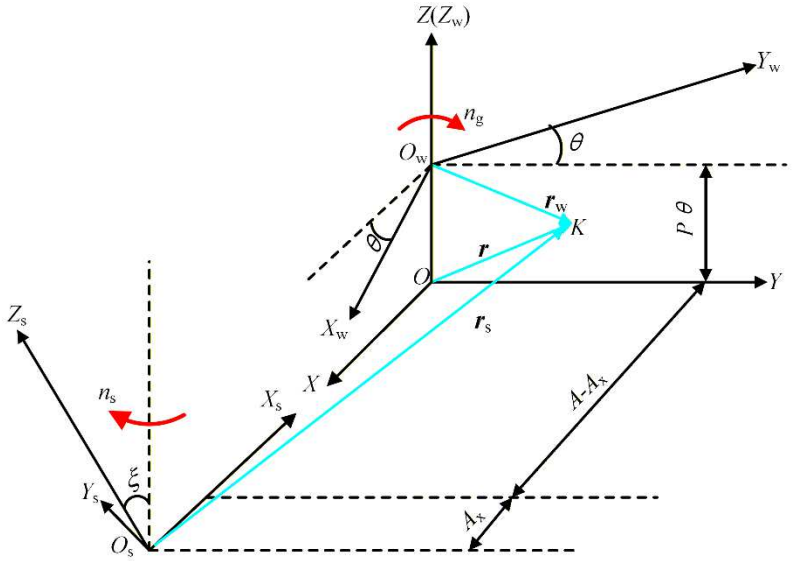


Fig.2 Spatial coordinate system describing wheel/gear meshing in helical gear form grinding

In Fig. 2, the instantaneous spatial contact point K between the wheel and the gear can be represented by the vectors $\boldsymbol{r}=(x,y,z)^T$, $\boldsymbol{r_w}=(x_w,y_w,z_w)^T$, and $\boldsymbol{r_s}=(x_s,y_s,z_s)^T$ with respect to the fixed, gear, and wheel coordinate systems, respectively.

The transformation from the gear coordinate system to the fixed coordinate system is given by:

$$\boldsymbol{r} = \boldsymbol{M}_z^{\theta}\boldsymbol{r}_w + P\theta\boldsymbol{k} \tag{1}$$

where the helical motion parameter is defined as $P=P_z/(2\pi)$, with P_z denoting the helical lead. $\boldsymbol{M}_z^{\theta}$ represents the rotation matrix corresponding to a clockwise rotation by an angle θ about the OZ-axis, can be expressed as:

$$\boldsymbol{M}_{\mathrm{z}}^{\theta}=\begin{bmatrix}\cos\theta & -\sin\theta & 0\\ \sin\theta & \cos\theta & 0\\ 0 & 0 & 1\end{bmatrix} \tag{2}$$

The transformation relation from the fixed coordinate system to the wheel coordinate system is mathematically represented as:

$$\boldsymbol{r}_{\mathrm{s}}=\boldsymbol{M}_{\mathrm{x}}^{\xi}\boldsymbol{r}-\left(A-A_{\mathrm{x}}\right)\boldsymbol{i}_{\mathrm{s}} \tag{3}$$

$$\boldsymbol{M}_{\mathrm{x}}^{\xi}=\begin{bmatrix}-1 & 0 & 0\\ 0 & -\cos\xi & \sin\xi\\ 0 & -\sin\xi & -\cos\xi\end{bmatrix} \tag{4}$$

where $\boldsymbol{M}_{\mathrm{x}}^{\xi}$ denotes the rotation matrix for a clockwise rotation by an angle ξ about the OX-axis.

3 Helical tooth surface model

The profile of a right-hand helical gear subjected to full-depth grinding consists of an involute flank surface and a root transition surface, as illustrated in Fig. 3. The helical tooth surface geometry is determined by the spatial meshing motion between the wheel and the gear. The geometry of the right-hand involute helical surface is expressed in terms of the rolling angle φ_{K} at an arbitrary grinding contact point:

$$\begin{cases}X_{\mathrm{w}}=r_{\mathrm{b}}\cos(\sigma_{\mathrm{b}}+\varphi_{\mathrm{K}}+\theta)+r_{\mathrm{b}}\varphi\sin(\sigma_{\mathrm{b}}+\varphi_{\mathrm{K}}+\theta)\\ Y_{\mathrm{w}}=r_{\mathrm{b}}\sin(\sigma_{\mathrm{b}}+\varphi_{\mathrm{K}}+\theta)-r_{\mathrm{b}}\varphi\cos(\sigma_{\mathrm{b}}+\varphi_{\mathrm{K}}+\theta)\\ Z_{\mathrm{w}}=P\theta\end{cases} \tag{5}$$

where r_{b} denotes the base circle radius, σ_{b} is defined as the half-angle corresponding to the tooth space on the base circle.

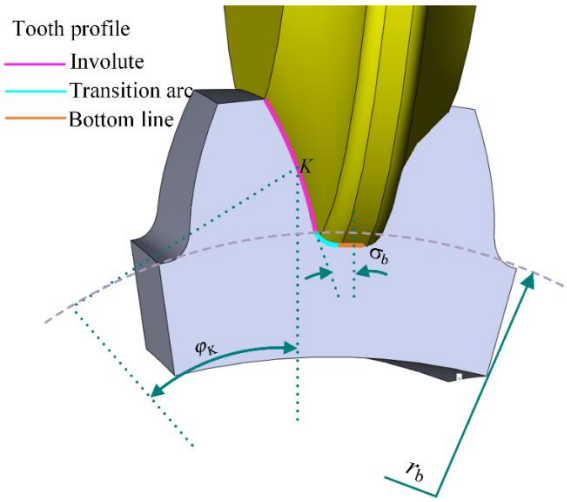


Fig.3 Helical tooth profile during form grinding

By modeling the root transition surface from the gear end face, the transition fillet helical surface is expressed as:

$$\begin{cases}X_{\mathrm{w}}=(x_{\mathrm{c}}+r_{\mathrm{f}}-r_{\mathrm{t}}\cos u)\cos\theta-(y_{\mathrm{c}}+r_{\mathrm{t}}\sin u)\sin\theta\\ Y_{\mathrm{w}}=(x_{\mathrm{c}}+r_{\mathrm{f}}-r_{\mathrm{t}}\cos u)\sin\theta+(y_{\mathrm{c}}+r_{\mathrm{t}}\sin u)\cos\theta\\ Z_{\mathrm{w}}=P\theta\end{cases} \tag{6}$$

where x_c and y_c denote the x- and y-coordinates of the transition fillet center, u represents the angular variable governing the transition arc geometry, r_f represents the root circle radius, and r_t defines the transition fillet radius.

4 Form grinding force model of helical gears

4.1 Normal geometrical contact model

During the form grinding of helical gears, the contact line between the wheel and the gear is a spatial curve whose geometry continuously varies as the grinding point moves across the tooth surface. Unlike spur gears, the contact condition in helical gear grinding cannot be simplified by the equivalent profile in the end plane. In this process, the wheel feeds along the helical path, while the normal plane of the helical gear is regarded as the theoretical reference plane, representing the designed geometric characteristics of the tooth flank. Although the contact line continuously changes with the local curvature radius, normal vector, and tangential direction at each grinding point, its overall evolution is still governed and constrained by the theoretical design geometry. As a result, the actual wheel–gear engagement region progressively approaches the theoretical normal plane, leading to the formation of the desired tooth profile.

The normal tooth profile of the helical gear at the pitch circle is equivalently represented by the form grinding contact curve. As illustrated in Fig.4, a point P is selected on the helical line of the pitch cylinder, and a normal plane N–N is established perpendicular to the helical line at this point. The intersection between the normal plane and the tooth surface defines the normal tooth profile. Figure 5 represents the geometric relation between the normal plane and the end plane, where plane ABB' represents the end plane and plane ACC' denotes the normal plane. In the figure, α_t and α_n denote the transverse pressure angle and the normal pressure angle, respectively, while β represents the helix angle.

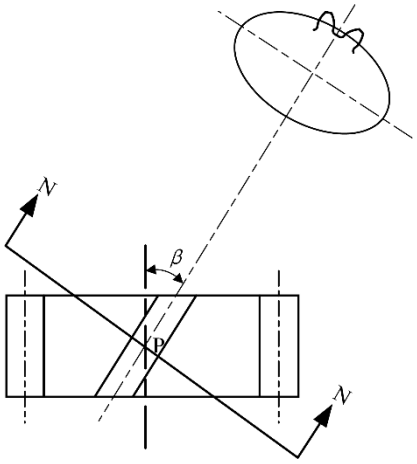


Fig.4 Normal tooth profile of the gear

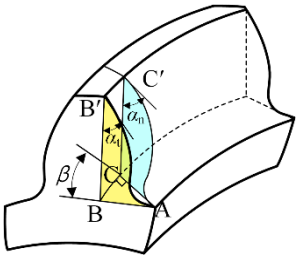


Fig.5 Geometric relationship between the normal plane and the end plane of the helical gear

The normal grinding depth represents the penetration of the grinding wheel into the workpiece

at the contact zone, serving as a key process parameter that characterizes the helical gear grinding process. Considering the kinematic relationship and geometric characteristics during helical gear form grinding, the contact geometries of the involute and fillet transition on the gear end surface are derived, as shown in Figs.6 and 7. According to the established geometric contact model and the spatial correspondence between the normal and end planes, the normal grinding depth at any contact point on the normal tooth profile is given by:

$$\begin{cases} a_{\mathrm{n,n1}} = a_{\mathrm{r}} \sin\left(\varphi_{\mathrm{K}} + \sigma_{\mathrm{b}}\right)\cos\beta \\ a_{\mathrm{n,n2}} = \left[a_{\mathrm{r}} \cos u + \sqrt{(a_{\mathrm{r}} \cos u)^2 - a_{\mathrm{r}}^2 + r_{\mathrm{t}}^2} - r_{\mathrm{t}} \right]\cos\beta \\ a_{\mathrm{n,n3}} = a_{\mathrm{r}} \cos\beta \end{cases} \tag{7}$$

where $a_{\mathrm{n,n1}}$, $a_{\mathrm{n,n2}}$, and $a_{\mathrm{n,n3}}$ denote the normal grinding depths corresponding to arbitrary contact points on the involute flank, fillet transition arc, and tooth root, respectively. a_{r} represents the wheel radial infeed depth, r_{a} denotes the addendum circle radius.

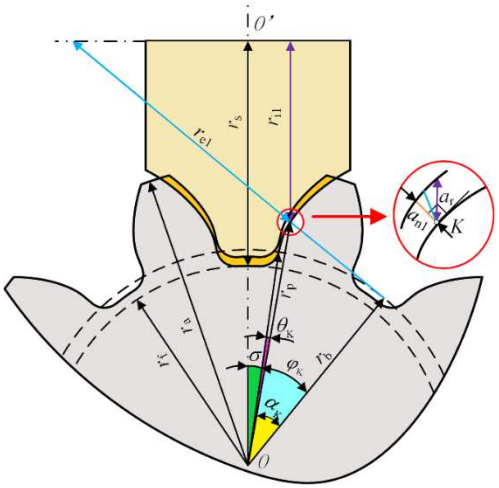


Fig.6 Grinding contact geometry of the tooth involute profile

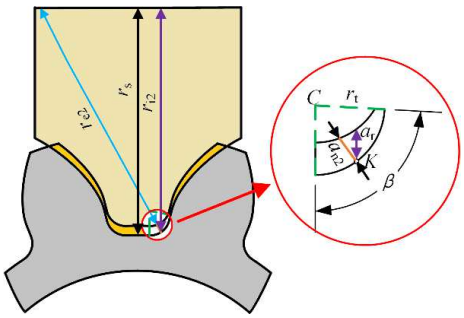


Fig.7 Geometric grinding contact relationship of the tooth fillet transition arc

In practice, the normal helical tooth profile does not strictly follow the canonical involute form. Tang et al. [19] has shown that the discrepancy between the normal profile of a helical gear and the transverse involute profile is negligible; hence the normal profile may be regarded as a locally modified involute. Accordingly, when formulating the theoretical form grinding force model of helical gears, the normal tooth profile outside the root fillet region is treated as an equivalent involute for computational purposes. This equivalence enables the use of standard involute-based geometric and kinematic relations in the force model while isolating the fillet transition for separate treatment.

The wheel equivalent radius represents the effective cutting radius that engages with the workpiece during form grinding. Based on the geometric contact model and the spatial relation between the normal and end planes, the equivalent radius between the normal tooth profile and the wheel forming contour is given by:

$$\begin{cases} r_{\mathrm{n,e1}} = \left[(r_{\mathrm{s}} + r_{\mathrm{f}} - \dfrac{r_{\mathrm{b}} \cos(\varphi_{\mathrm{K}} - \arctan\varphi_{\mathrm{k}} + \sigma_{\mathrm{b}})}{\cos(\arctan\varphi_{\mathrm{k}})}) \Big/ \sin(\varphi_{\mathrm{k}} + \sigma_{\mathrm{b}}) \right] \cos\beta \\ r_{\mathrm{n,e2}} = \dfrac{\left[r_{\mathrm{s}} - r_{\mathrm{t}}(1-\cos u) \right] \cos\beta}{\cos u} \\ r_{\mathrm{n,e3}} = r_{\mathrm{s}} \cos\beta \end{cases} \tag{8}$$

where $r_{n,\mathrm{e1}}$, $r_{n,\mathrm{e2}}$, and $r_{n,\mathrm{e3}}$ denote the equivalent radii at arbitrary positions on the involute flank, fillet transition arc, and tooth root of the normal profile, respectively. r_{s} represents the wheel initial radius prior to material removal.

The wheel normal linear velocities corresponding to the involute, fillet transition arc, and tooth root, denoted as $v_{\mathrm{n,s1}}$, $v_{\mathrm{n,s2}}$, and $v_{\mathrm{n,s3}}$, respectively, can be determined as:

$$\begin{cases} v_{\mathrm{n,s1}} = \dfrac{2n_{\mathrm{s}}\pi r_{\mathrm{n,e1}} \sin\left(\varphi_{\mathrm{k}} + \sigma_{\mathrm{b}}\right) \cos\beta}{60\times1000} \\ v_{\mathrm{n,s2}} = \dfrac{2n_{\mathrm{s}}\pi r_{\mathrm{n,e2}} \cos u \cos\beta}{60\times1000} \\ v_{\mathrm{n,s3}} = \dfrac{2n_{\mathrm{s}}\pi r_{\mathrm{n,e3}} \cos\beta}{60\times1000} \end{cases} \tag{9}$$

As illustrated in Fig.8, an infinitesimal segment is taken along the tooth involute for analysis. When the rolling angle increases by an infinitesimal increment dφ, the corresponding arc length increment of the involute, dl_1, can be expressed as:

$$\mathrm{d}l_1 = KK' = \overline{EK}\mathrm{d}\varphi = DE\mathrm{d}\varphi = r_{\mathrm{b}}\varphi\mathrm{d}\varphi \tag{10}$$

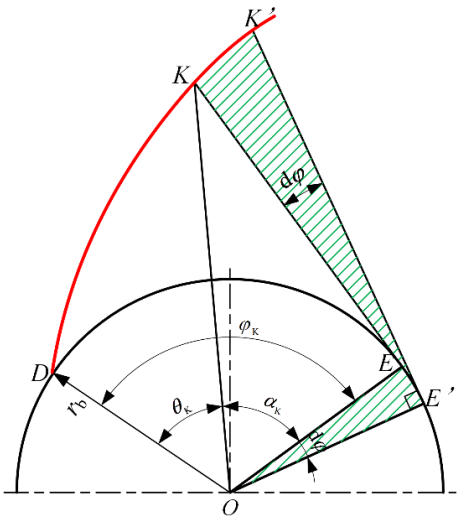


Fig.8 An infinitesimal segment on the tooth involute profile

Similarly, the arc length increment of the fillet transition curve can be expressed as:

$$\mathrm{d}l_2 = r_\mathrm{t} u \mathrm{d}u \tag{11}$$

For the tooth root, the corresponding linear length can be expressed as:

$$l_3 = r_\mathrm{b} \sin\sigma_\mathrm{b} - r_\mathrm{t} \sin u \tag{12}$$

4.2 Form grinding force model

By incorporating the unit-width force model for plane grinding [20], the helical gear form grinding force is derived through the integration of incremental forces over the wheel–gear engagement length. Accordingly, the grinding force for helical gear form grinding can be expressed as:

$$\begin{cases} F_\mathrm{t} = F_{\mathrm{t}1} + F_{\mathrm{t}2} + F_{\mathrm{t}3} \\ F_\mathrm{n} = F_{\mathrm{n}1} + F_{\mathrm{n}2} + F_{\mathrm{n}3} \end{cases} \tag{13}$$

$$\begin{cases} F_{\mathrm{t}1} = \int_0^{\varphi_{\max}} (K_1 + K_2 \ln(\dfrac{v_{\mathrm{n,s}1}^{1.5}}{a_{\mathrm{n,n}1}^{0.25} v_\mathrm{w}^{0.5}})) \dfrac{v_\mathrm{w} a_{\mathrm{n,n}1}}{v_{\mathrm{n,s}1}} r_\mathrm{b} \varphi \mathrm{d}\varphi + \int_0^{\varphi_{\max}} (\alpha_1 + \dfrac{v_\mathrm{w}}{r_{\mathrm{n,e}1} v_{\mathrm{s}1}} \beta_1) \sqrt{2 r_{\mathrm{n,e}1} a_{\mathrm{n,n}1}}\, r_\mathrm{b} \varphi \mathrm{d}\varphi \\ F_{\mathrm{t}2} = \int_0^{u_{\max}} (K_1 + K_2 \ln(\dfrac{v_{\mathrm{n,s}2}^{1.5}}{a_{\mathrm{n,n}2}^{0.25} v_\mathrm{w}^{0.5}})) \dfrac{v_\mathrm{w} a_{\mathrm{n,n}2}}{v_{\mathrm{n,s}2}} r_\mathrm{t} u \mathrm{d}u + \int_0^{u_{\max}} (\alpha_1 + \dfrac{v_\mathrm{w}}{r_{\mathrm{n,e}2} v_{\mathrm{n,s}2}} \beta_1) \sqrt{2 r_{\mathrm{n,e}2} a_{\mathrm{n}2}}\, r_\mathrm{t} u \mathrm{d}u \\ F_{\mathrm{t}3} = \int_0^{l_3} (K_1 + K_2 \ln(\dfrac{v_{\mathrm{n,s}3}^{1.5}}{a_{\mathrm{n,n}3}^{0.25} v_\mathrm{w}^{0.5}})) \dfrac{v_\mathrm{w} a_{\mathrm{n,n}3}}{v_{\mathrm{n,s}3}} \mathrm{d}l_3 + \int_0^{b} (\alpha_1 + \dfrac{v_\mathrm{w}}{r_{\mathrm{n,e}3} v_{\mathrm{n,s}3}} \beta_1) \sqrt{2 r_{\mathrm{n,e}3} a_{\mathrm{n,n}3}}\, \mathrm{d}l_3 \end{cases} \tag{14}$$

$$\begin{cases} F_{\mathrm{n}1} = \int_0^{\varphi_{\max}} (K_3 + K_4 \ln(\dfrac{v_{\mathrm{n,s}1}^{1.5}}{a_{\mathrm{n,n}1}^{0.25} v_\mathrm{w}^{0.5}})) \dfrac{v_\mathrm{w} a_{\mathrm{n,n}1}}{v_{\mathrm{n,s}1}} r_\mathrm{b} \varphi \mathrm{d}\varphi + \int_0^{\varphi_{\max}} \dfrac{v_\mathrm{w}}{v_{\mathrm{n,s}1}} \varepsilon_1 \sqrt{\dfrac{a_{\mathrm{n,n}1}}{2 r_{\mathrm{n,e}1}}}\, r_\mathrm{b} \varphi \mathrm{d}\varphi \\ F_{\mathrm{n}2} = \int_0^{u_{\max}} (K_3 + K_4 \ln(\dfrac{v_{\mathrm{n,s}2}^{1.5}}{a_{\mathrm{n,n}2}^{0.25} v_\mathrm{w}^{0.5}})) \dfrac{v_\mathrm{w} a_{\mathrm{n,n}2}}{v_{\mathrm{n,s}2}} r_\mathrm{t} u \mathrm{d}u + \int_0^{u_{\max}} \dfrac{v_\mathrm{w}}{v_{\mathrm{n,s}2}} \varepsilon_1 \sqrt{\dfrac{a_{\mathrm{n,n}2}}{2 r_{\mathrm{n,e}2}}}\, r_\mathrm{t} u \mathrm{d}u \\ F_{\mathrm{n}3} = \int_0^{l_3} (K_3 + K_4 \ln(\dfrac{v_{\mathrm{n,s}3}^{1.5}}{a_{\mathrm{n,n}3}^{0.25} v_\mathrm{w}^{0.5}})) \dfrac{v_\mathrm{w} a_{\mathrm{n,n}3}}{v_{\mathrm{n,s}3}} \mathrm{d}l_3 + \int_0^{b} \dfrac{v_\mathrm{w}}{v_{\mathrm{n,s}3}} \varepsilon_1 \sqrt{\dfrac{a_{\mathrm{n,n}3}}{2 r_{\mathrm{n,e}3}}}\, \mathrm{d}l_3 \end{cases} \tag{15}$$

The coefficients K_1, K_2, K_3, K_4, α_1, β_1, and ε_1 are empirical parameters that must be determined through experimental calibration.

5. Experimental Measurement of Form Grinding Forces in Helical Gears

5.1 Experimental setup and measurement procedure

Form grinding experiments on helical gears were conducted using a Gleason–PFAUTER P600/800G h form grinding machine. This machine allows four-axis simultaneous motion (C, X, Y, and Z) and achieves a grinding accuracy of up to DIN Grade 4. Prior to grinding, the wheel **(**Φ350 × 32 × 127 mm, 3SG70GHV50**)** was precisely dressed using a diamond roller to ensure accurate wheel geometry, as shown in Fig.9. The wheel was composed of SG ceramic microcrystalline abrasive with a grit size of #70 and a vitreous bond**.** Compared with conventional alumina wheels, SG ceramic abrasive wheels exhibit higher grinding ratio, hardness, and toughness, as well as excellent self-sharpening characteristics, making them particularly suitable for achieving high dimensional accuracy in form grinding of hardened gear steels. The test workpiece was a carburized, quenched, and tempered involute helical gear made of 17CrNiMo6 steel. Details of the gear geometry and its chemical composition are presented in Tables1 and 2.

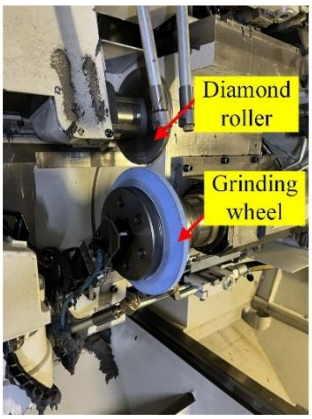


Fig.9 Dressing process of the form grinding wheel

Table 1 Geometrical parameters of the workpiece

Parameter / Unit	Value
Number of teeth	20
Normal module / mm	9.5
Helix angle / (°)	16
Normal pressure angle / (°)	20
Face width / mm	40

Table 2 Chemical composition of 17CrNiMo6 steel

Element	C	Si	Mn	Cr	Ni	Mo
Mass fraction / %	0.19	0.3	0.85	1.5	1.6	0.27

The grinding forces were measured by a KISTLER–9129AA multi-component dynamometer. This dynamometer is capable of simultaneously measuring forces in three orthogonal directions, satisfying the requirements for precision grinding experiments. The force signals generated by the dynamometer are transmitted to a KISTLER–5167A charge amplifier equipped with an integrated DAQ system, where the charges induced by the applied forces are amplified and converted into voltage signals. These signals are then transferred to a computer for data acquisition and analysis. Figure 10 illustrates the grinding force measurement system for the helical gear.

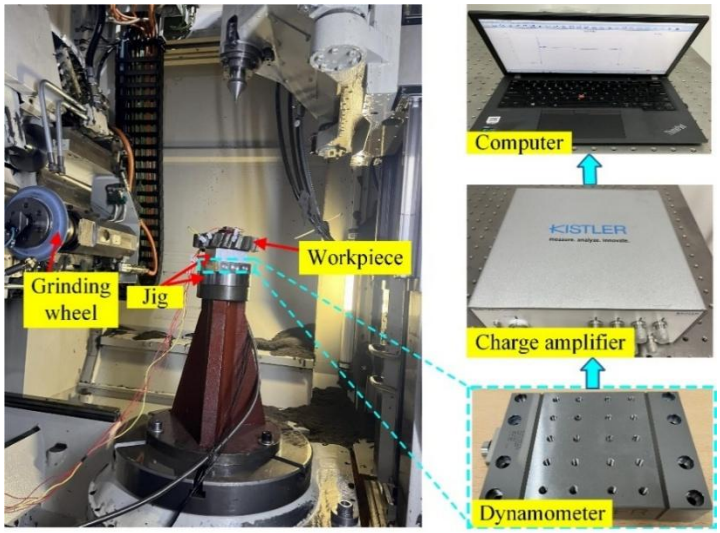


Fig.10 Experimental setup for measuring form grinding forces of the helical gear

Since the coolant could not be switched off during the experiment, force signals were recorded under both grinding and non-grinding conditions to eliminate the influence of fluid impact on the measured results. The fluid-induced disturbance was subsequently removed from the actual grinding force data. Figure 11 presents a representative set of grinding force curves obtained by grinding test, conducted with the parameters v_s=25 m/s, a_r=0.02 mm, v_w=1500 mm/min, and n_g=20 rad/min. Here, F_t denotes the tangential force parallel to the feed motion, and F_n denotes the normal force perpendicular to the feed motion. During the grinding cycle, the force increases as the wheel engages the gear, remains stable during steady-state grinding, and then decreases rapidly as the wheel disengages from the gear.

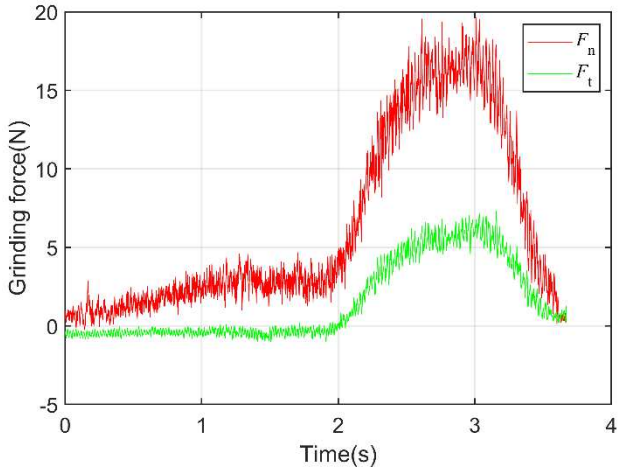


Fig.11 Measured grinding force results

5.2 Parameter calibration of the form grinding force model

Within the helical gear form grinding force model, seven constants—K_1, K_2, K_3, K_4, α_1, β_1, and ε_1 in Equations (14) and (15) must be determined experimentally. Table 3 presents four sets of grinding parameters and the corresponding measured grinding forces. For each condition, three repeated trials were conducted, and the mean value was taken. By substituting the experimental results into a system of multiple linear equations, the unknown parameters were obtained, as summarized in Table 4.

Table 3 Experimental combinations and corresponding grinding force results

v_s (m/s)	v_w (mm/min)	a_r (mm)	n_g (rad/min)	F_n (N)	F_t (N)
30	1000	0.03	20	21.53	6.22
25	1500	0.01	20	12.65	3.65
20	2000	0.03	20	32.19	10.57
25	1500	0.02	20	19.07	5.96

Table 4 Experimentally determined constants of the grinding force model

K_1	K_2	K_3	K_4	α_1	β_1	ε_1
−7609	1357	−766675	57760	0.051	538	38260

By substituting the experimentally determined constants listed in Table 4 into Eqs. (13)–(15), the complete theoretical model for the grinding forces during helical gear form grinding is obtained.

6. Model validation and results analysis

6.1 Verification of the form grinding force model

To evaluate the proposed grinding force model and assess the effects of individual process

parameters, single-factor experiments were conducted under different machining conditions. Figs. 12–14 present the variations in grinding forces with respect to grinding depth, wheel speed, and feed rate. The calculated forces closely match the experimental measurements, with both showing similar variation tendencies, demonstrating the validity and reliability of the proposed theoretical model. Furthermore, the experimentally measured forces are slightly higher than the theoretical predictions. This discrepancy arises mainly from grinding wheel wear, which increases the friction coefficient at the grain-workpiece interface and consequently increases the grinding force. In addition, irregular deformation of worn grains extends the effective contact arc and raises the instantaneous material removal rate, thereby increasing the grinding forces.

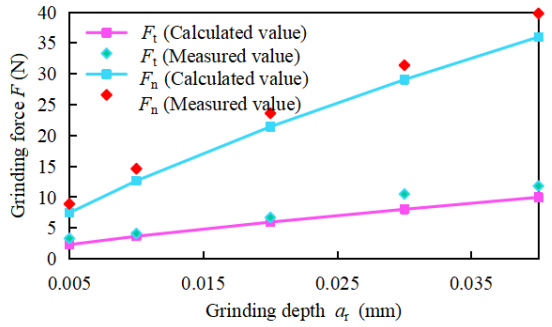


Figure 12 Relationship between grinding depth and grinding force (v_s=25 m/s, v_w=1500 mm/min)

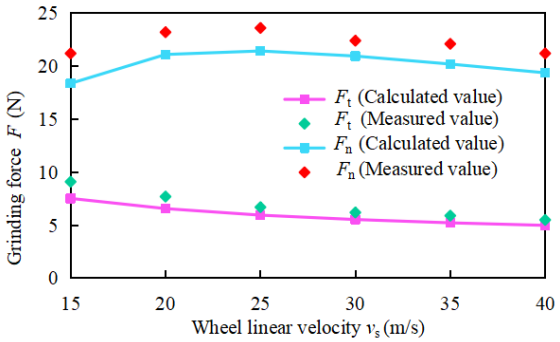


Figure 13 Relationship between wheel linear velocity and grinding force (a_r=0.02 mm, v_w=1500 mm/min)

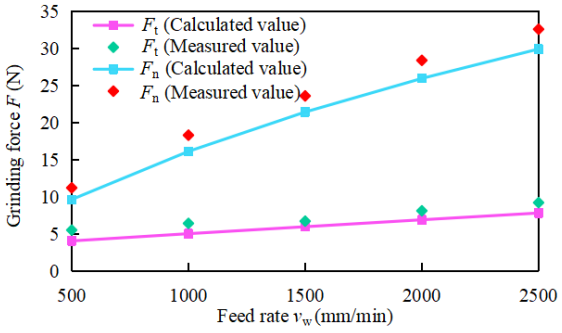


Figure 14 Relationship between feed rate and grinding force (a_r=0.02 mm, v_s=25 m/s)

6.2 Processing parameter influence on grinding force

According to Figure 12, an increase in grinding depth a_r from 0.005 mm to 0.04 mm results in a substantial growth in the predicted forces: F_t rises from 2.29 N to 9.98 N, and F_n increases from 7.45 N to 35.98 N. This trend confirms a positive dependence of the grinding force on a_r, with the

force magnitude increasing as the grinding depth grows. This is because the increase in a_r activates more cutting grains, which in turn enlarges the effective wheel-workpiece contact arc length. From the perspective of cutting mechanics, an elevated material removal rate enhances chip-formation resistance and strengthens grain-workpiece friction, which collectively raises the grinding force.

From Fig.13, it can be observed that as the wheel linear velocity v_s varies from 15 m/s to 40 m/s, F_t ranges from 7.53 N to 4.99 N, and F_n ranges from 21.43 N to 18.37 N. The results show that F_t decreases with increasing v_s, while F_n first increases and then decreases. This trend arises because a higher v_s introduces more abrasive grains into engagement per unit time, which diminishes the maximum undeformed chip thickness of individual grains, thereby reducing the effective grinding force per grain. In addition, the higher v_s increases the workpiece surface temperature, enhancing thermal softening and promoting plastic flow, which in turn lowers the grinding force required for material removal. However, when v_s is within the lower range of 15–25 m/s, the longer interaction time between the grains and workpiece enhances static frictional resistance, resulting in an increase in F_n. Furthermore, at lower grinding speeds, larger chips are generated, and their motion encounters greater resistance, further increasing F_n. As v_s continues to rise, the relative sliding speed between the abrasive grains and the workpiece increases, reducing both static friction and chip resistance, thereby causing F_n to decrease.

As shown in Fig.14, when the workpiece feed rate v_w increases from 500 mm/min to 2500 mm/min, the calculated F_t increases from 4.14 N to 7.80 N, while F_n rises from 9.63 N to 29.93 N. This indicates that both grinding force components increase with rising v_w. This trend is attributed to the fact that a higher feed rate produces larger undeformed chip thicknesses per abrasive grain, enhancing the material removal rate and consequently increasing the grinding forces.

6.3 Non-uniform distribution of grinding forces

To further analyze the force distribution over the full tooth depth, the established theoretical model was employed to evaluate the tangential and normal forces at various positions on the helical tooth profile, as shown in Figs. 15–17. The gear geometry is listed in Table 2, while the grinding conditions for the analysis were defined as a_r=0.02 mm, v_s=25 m/s, and v_w=1500 mm/min.

According to Fig.15, the grinding force demonstrates an upward trend along the involute profile with increasing rolling angle. A higher force is observed at the tooth top compared with the area close to the intersection between the involute profile and the base circle. From Fig.16, the grinding force decreases as the arc angle increases, indicating that the grinding force becomes larger toward the tooth root. From Fig.17, the grinding force in the root region remains almost constant and is significantly greater than that in both the involute and transition arc regions.

As dictated by the geometric contact relations in the grinding zone, the normal grinding depth grows as the rolling angle increases and declines as the transition arc angle becomes larger. Therefore, the smallest normal grinding depth occurs at the intersection between the tooth profile and base circle, while the largest occurs at the tooth root. Owing to the position-dependent variation of normal grinding depth and its direct contribution to grinding force generation, the grinding force demonstrates a clear non-uniform distribution over the complete tooth depth. The grinding force is minimal near the base circle and maximal at the tooth root.

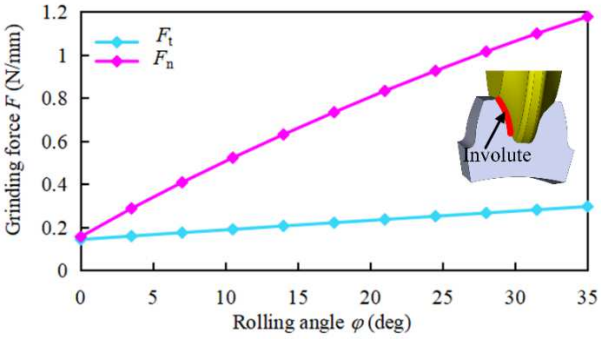


Figure 15 Grinding force distribution along the involute

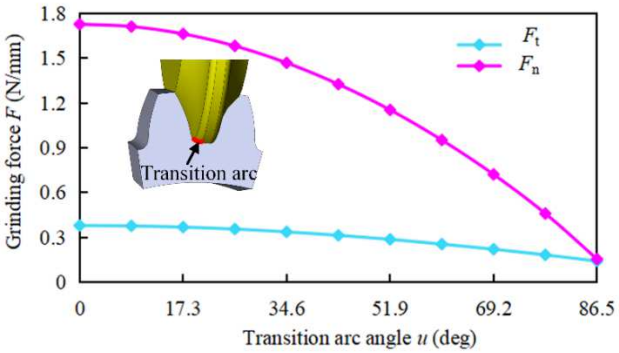


Figure 16 Grinding force distribution along the transition arc

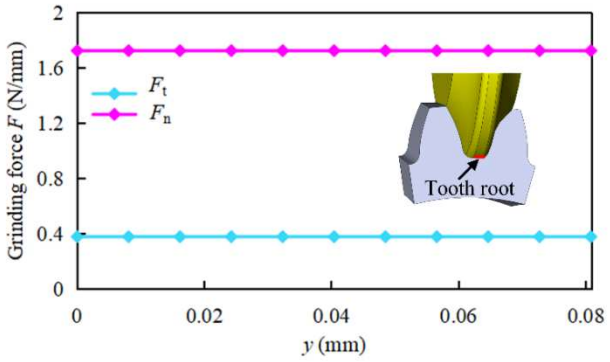


Figure 17 Grinding force distribution along the tooth root

7 Conclusions

To investigate the distribution and variation of grinding forces during helical gear form grinding, a theoretical force model was proposed and experimentally validated. Based on this, the effects of grinding parameters on both the magnitude and the non-uniform distribution of grinding forces along the tooth profile were thoroughly examined. The main conclusions can be summarized as follows:

(1) A theoretical model for predicting grinding forces during helical gear form grinding was proposed by integrating the spatial kinematic model and geometric contact relationships. The experimental constants in the model were determined through grinding experiments. By comparing the calculated and measured forces under different processing conditions, good agreement and consistent trends were observed, thereby confirming the validity of the proposed model.

(2) The influence of processing parameters on grinding forces was investigated using single-factor experiments. Both theoretical and experimental results indicate that the normal and tangential grinding forces increase with the grinding depth and workpiece feed rate. As the wheel speed

increases, the tangential grinding force decreases, while the normal grinding force first increases and then decreases.

(3) Using the developed theoretical model, the tangential and normal grinding forces along the tooth profile were calculated to elucidate the impact of tooth geometry on force distribution. The results reveal that both forces increase with the involute rolling angle and decrease with the transition arc angle. Along the involute, the grinding force is largest at the tooth top and smallest near the base circle. Along the transition arc, the grinding force increases toward the tooth root. In the root region, the grinding force remains nearly constant due to the uniform grinding depth. Overall, the grinding force exhibits a distinct non-uniform distribution along the helical tooth profile, being minimal at the base circle and maximal at the tooth root.

Author contribution All the authors contributed to the study conception and design. Material preparation, data collection, and analysis were performed by Shuying YANG. The first draft of the manuscript was written by Shuying YANG and Lei ZHENG, and all the authors commented on previous versions of the manuscript. All the authors read and approved the final manuscript.

Funding This work was support by the General Project of Basic Science (Natural Science) Research in Higher Education Institutions of Jiangsu Province (No.25KJB460020) and General Project of Philosophy and Social Science Research Program in Higher Education Institutions of Jiangsu Province (No.2025SJYB1063).

Data availability All data and parameters for the simulation model used in this paper have been provided.

Declarations

Ethics approval The authors state that the present work is in compliance with the ethical standards.

Consent to participate All the authors consent to participate this work.

Consent for publication All authors agree to publish.

Competing interests The authors declare no competing interests.

References

[1] Ding S, Chen ZW，Zhang H, et al. Gear evaluation deviations-based crucial geometric error identification of five-axis CNC gear form grinding process. Journal of Manufacturing Processes 2023; 99: 663–675.

[2] Ma XF, Cai ZQ, Yao B, et al. Dynamic grinding force model for face gear based on the wheel-gear contact geometry. Journal of Materials Processing Technology 2022; 306:117633.

[3] Ma C, Wang JL, Zhang MJ, et al. Prediction of Grinding Force by an Electroplated Grinding Wheel with Orderly-Micro-Grooves. Chinese Journal of Mechanical Engineering 2023; 36 (1):1–12.

[4] Li HB, Chen T, Duan ZY, et al. A grinding force model in two-dimensional ultrasonic-assisted grinding of silicon carbide. Journal of Materials Processing Technology 2022; 304: 117568.

[5] Zhang YB, Gong P, Tang LZ, et al. Topography Modeling of Surface Grinding Based on Random Abrasives and Performance Evaluation. Chinese Journal of Mechanical Engineering 2024; 37 (1) :1–24.

[6] Chen T, Wang XW, Zhao B, et al. Surface integrity evolution during creep feed profile grinding of c-TiAl blade tenon. Chinese Journal of Aeronautics 2024; 37(8): 496–512.

[7] Qian N, Fu YC, Chen JJ, et al. Axial rotating heat-pipe grinding wheel for eco-benign machining: A novel method for dry profile-grinding of Ti-6Al-4V alloy. Journal of Manufacturing Processes 2020; 56: 216–227.

[8] Ardashev DV, Dyakonov AA. Mathematical model of the grinding force with account for blunting of abrasive grains of the grinding wheel. Journal of Manufacturing Science and Engineering-Transactions of the ASME 2017; 139:1–7.

[9] Li BK, Ding WF, Zhu YJ, et al. Thermal analysis on profile grinding of turbine disc slots of powder metallurgy

superalloy FGH96. International Communications in Heat and Mass Transfer 2024; 159: 108207.

[10] Miao Q, Ding WF, Kuang WJ, et al. Grinding force and surface quality in creep feed profile grinding of turbine blade root of nickel-based superalloy with microcrystalline alumina abrasive wheels. Chinese Journal of Aeronautics 2021; 34(2): 576–585.

[11] Wu H, Yao ZQ. Force modeling for 2D freeform grinding with infinitesimal method. Journal of Manufacturing Processes 2021; 70: 108–120.

[12] Zhao CY, Li JY, Liu YM. Study on the grinding force of single grain in rail grinding based on pen-type belt grinding. Journal of Manufacturing Processes 2023; 99:749–811.

[13] Wen J, Zhou WH, Tang JY, et al. Residual stress evolution for tooth double-flank by gear form grinding. Journal of Manufacturing Processes 2022; 77:754–769.

[14] Xiao YL, Wang SL, Ma C, et al. Grinding force model for gear profile grinding based on material removal mechanism. International Journal of Advanced Manufacturing Technology 2023; 125:743–762.

[15] Bie WB, Zhao B, Gao GF, et al. Two-dimensional ultrasonic vibration-assisted dry grinding gear: grinding force and surface characteristics. International Journal of Advanced Manufacturing Technology 2024; 131:3021–3038.

[16] Yi J, Jin T, Zhou W, et al. Theoretical and experimental analysis of temperature distribution during full tooth groove form grinding. Journal of Manufacturing Processes 2020; 58: 101–115.

[17] Yi J, Pei KL, Li ZH, et al. Numerical and experimental investigation on temperature field during small-module gear creep feed deep profile grinding. International Journal of Advanced Manufacturing Technology 2024;132 (9–10): 4965–4977.

[18] Yang SY, Liang RJ, Chen WF, et al. Modelling and experiment for grinding forces of gear form grinding considering complete tooth depth engagement. Proceedings of the Institution of Mechanical Engineers, Part B, Journal of Engineering Manufacture 2022; 236(13): 1738–1750.

[19] Yang SY, Chen WF, Zheng L. On the grinding temperature field of helical gears: Modeling and experiments. Journal of Manufacturing Processes 2024;124: 1010–1024.

[20] Tang JY, Du J, Chen YP. Modeling and experimental study of grinding forces in surface grinding. Journal of Materials Processing Technology 2009; 209(6): 2847–2854.

[21] Malkin S, Cook N H. The wear of grinding wheels, part 1, attritions Wear. Transactions of the ASME, Journal of Engineering for Industry, Series B, 1971; 93: 1120–1133.